Dalton Transactions

# The non-centrosymmetric layered compounds IrTe2I and RhTe2I

| | |
|---|---|
| Journal: | *Dalton Transactions* |
| Manuscript ID | DT-ART-04-2022-001224.R1 |
| Article Type: | Paper |
| Date Submitted by the Author: | 12-May-2022 |
| Complete List of Authors: | Ni, Danrui; Princeton University, Chemistry<br>Gui, Xin; Princeton University, Chemistry<br>Han, Bingzheng; Princeton University, Physics<br>Wang, Haozhe; Rutgers University Department of Chemistry and Chemical Biology<br>Xie, Weiwei; Rutgers University, Chemistry; Louisiana State University, Chemistry<br>Ong, N.; Princeton University, Physics<br>Cava, Robert; Princeton University, Department of Chemistry |
| | |

SCHOLARONE™
Manuscripts

# The non-centrosymmetric layered compounds $IrTe_2I$ and $RhTe_2I$

Danrui Ni[a], Xin Gui[a], Bingzheng Han[b], Haozhe Wang,[c] Weiwei Xie,[c] N. P. Ong[b], and R. J. Cava*[a]

[a]Department of Chemistry, Princeton University, Princeton, NJ 08544, United States

[b]Department of Physics, Princeton University, Princeton, NJ 08544, United States

[c]Department of Chemistry and Chemical Biology, Rutgers University, Piscataway, NJ 08854, USA

**Abstract**

The previously unreported layered compounds $IrTe_2I$ and $RhTe_2I$ were prepared by a high-pressure synthesis method. Single crystal X-ray and powder X-ray diffraction studies find that the compounds are isostructural, crystallizing in a layered orthorhombic structure in the non-centrosymmetric, non-symmorphic space group $Pca2_1$ (#29). Characterization reveals diamagnetic, high resistivity, semiconducting behavior for both compounds, consistent with the +3 chemical valence and $d^6$ electronic configurations for both iridium and rhodium and the Te-Te dimers seen in the structural study. Electronic band structures are calculated for both compounds, showing good agreement with the experimental results.

**Keywords:**

High-pressure synthesis; Heavy metal chalcohalides; Layered structure; Telluroiodide of iridium and rhodium.

## 1. Introduction

Inorganic heavy metal compounds based on halogens and/or chalcogens have been studied for decades due to their electronic and magnetic properties and multiple potential applications. This family includes thermoelectric materials,[1–3] applications in photovoltaic devices[4,5] and radiation detectors,[6,7] and quantum materials[8–11] for example. Especially of recent interest have been heavy transition metal chalcogenides or halides with layered crystal structures, as their resulting pseudo 2D electronic and magnetic systems, together with the Van der Waals forces between the layers, provide both a platform for studying forefront spin/electron interactions, and for further fabrication and modification.[12–15] In recent years, many layered compounds containing Group VIII elements (such as ruthenium, rhodium, and iridium), are of great research interest, and have been studied as candidates for quantum spin liquids, topological insulators, and superconductors.[16–19]

In this report, we describe layered $IrTe_2I$ and $RhTe_2I$, prepared by a high-pressure solid-state method. These compounds have not been reported previously, and do not appear to form using an ambient pressure high temperature synthesis method. With the help of high pressure, which often results in denser phases, uncommon structural features, and some pressure-induced properties,[20–23] we find that these materials crystallize in a new layered structure. The structure is refined in the $Pca2_1$ space group, which is both nonsymmorphic and noncentrosymmetric, by single crystal and powder X-ray diffraction. Te-Te bonding is found in the structure, which is consistent with the $d^6$ configuration of Rh(III) and Ir(III), and the diamagnetic behavior and high resistivities of the compounds. Both experimental results and theoretical calculations suggest a semiconducting nature for the two compounds. Their non-centrosymmetric, non-symmorphic layered structure may trigger further interest in the band structures and physical properties of the compounds.

## 2. Experimental

**Material Synthesis:** The compounds were prepared using a solid-state high pressure synthesis method. Stoichiometric elementary iridium (Alfa Aesar 99.9%) or rhodium powders (Alfa Aesar 99.95%), tellurium pieces (Alfa Aesar 99.9999%), and iodine (Alfa Aesar 99.99+%, resublimed for purification) were pre-mixed and loaded in a boron nitride crucible. The assembly was then inserted into a pyrophillite cube and pressed to a pressure of 6 GPa with a cubic multi-anvil system (Rockland Research Corporation). After the pressure was applied, the material was heated to 800 - 900 °C at

50 °C/min and held at the desired temperature for 1 hour. The temperature was determined by an internal thermocouple. The system was quench-cooled before depressurizing, and small crystals found in the post-reaction polycrystalline products were saved for single crystal X-ray diffraction (SXRD) measurements.

**Crystal structure determination:** Multiple $IrTe_2I$ and $RhTe_2I$ crystals (~80×80×15 $\mu m^3$), cleaved from as-made samples, were studied by SXRD to determine the crystal structure. The structure, consistent among all crystals, was determined using a Bruker D8 QUEST diffractometer equipped with APEX III software and Mo radiation ($\lambda_{Ka}$= 0.71073 Å) at room temperature. The crystals were mounted on a Kapton loop. Data acquisition was made *via* the Bruker SMART software with corrections for Lorentz and polarization effects included. A numerical absorption correction based on crystal-face-indexing was applied through the use of *XPREP*. The direct method and full-matrix least-squares on $F^2$ procedures within the SHELXTL package were employed to solve the crystal structure.[24,25] The SXRD data for $RhTe_2I$ were successfully collected and refined, while the $IrTe_2I$ samples were too polycrystalline to generate high-quality single crystal diffraction data. Thus laboratory powder X-ray diffraction (PXRD) patterns were collected on a Bruker D8 Advance Eco diffractometer with Cu Kα radiation (λ= 1.5418 Å) to quantitatively determine its structure. A Rietveld refinement using GSAS II software was conducted on the PXRD data from polycrystalline $IrTe_2I$, and a preliminary structure was obtained. (In such refinements the thermal parameters for the atoms have no detailed meaning aside from indicating that the structure solution is well-behaved.) A Le Bail fit of $RhTe_2I$ PXRD pattern was carried out via the TOPAS software to confirm the uniformity of the bulk material.

**Property Characterization:** The temperature-dependent and field-dependent magnetization (M) data were collected on a Quantum Design (QD) Physical Property Measurement System (PPMS), using an ACMS option. The magnetic susceptibility was defined as M/H. Electrical transport measurements were carried out on QD PPMS Dynacool, with phosphor bronze wires (for $IrTe_2I$) and platinum wires (for $RhTe_2I$) attached to samples using silver paint. No indication of reaction of the silver paint with the sample was observed during the measurements.

Magnetoresistance measurements were conducted on $IrTe_2I$ polycrystalline pieces at applied magnetic fields up to 9 T. A Keithley 2400 Source was used to perform two-probe resistivity measurements in the constant voltage ($V$) mode. The sample resistance is therefore given by $R = V / I$.

The diffuse reflectance data were collected at ambient temperature on a Cary 5000i UV-VIS-NIR spectrometer with an internal DRA-2500 integrating sphere. The reflectance data were transferred to pseudo absorbance using Kubelka-Munk theory and the band gap values were calculated from the Tauc plots[26].

**Electronic Structure calculation:** Density Functional Theory (DFT) calculations with the projector augmented-wave (PAW)[27] method were performed using the Vienna Ab initio Simulation Package (VASP)[28] version 5.4.4. The generalized gradient approximation (GGA) parameterized Perdew-Burke-Ernzerhof (PBE) functional[29] was used to account for the electronic exchange and correlation. A kinetic energy cutoff of 400 eV was used for the plane-wave basis set. Γ-point centered Monkhorst–Pack[30] *k*-point grids of 8 × 4 × 8 and 12 × 6 × 12 were applied to sample the Brillouin zone for the self-consistent field calculation and density of states (DOS), respectively. Spin-orbit coupling (SOC) was included in the calculations once specified. The structures were relaxed until the maximum absolute total force on each atom was smaller than $10^{-3}$ eV/Å and the energy converged to $10^{-8}$ eV.

## 3. Results and Discussion

Samples of $IrTe_2I$ and $RhTe_2I$ were prepared by solid-state high-pressure synthesis. High yields were obtained for both compounds through one-hour annealing at 800 °C and 6 GPa. No oxidic impurities were observed in either sample, however a small amount of $RhTe_2$ was found as an impurity in the post-reaction $RhTe_2I$ product. This small amount of impurity could not be eliminated when 10% excess iodine was used under the same conditions. The compounds are isostructural, with an orthorhombic unit cell in the non-centrosymmetric non-symmorphic space group $Pca2_1$. ($IrTe_2I$: $a$ = 6.362 Å, $b$ = 10.57 Å, $c$ = 6.405 Å, $Z$ = 4; $RhTe_2I$: $a$ = 6.368 Å, $b$ = 10.56 Å, $c$ = 6.416 Å, $Z$ = 4), which is exhibited in **Figure 1**. (In other words, there is no inversion center in their structures, and no point that can be defined such that all symmetries present are the product of a symmetry that fixes this point plus a lattice translation.) Both non-centrosymmetric and non-symmorphic crystal structures have been postulated to give rise to topological physics[31,32], but the study of topological properties is not the aim of the current research. These two compounds can't be formed using the solid-state preparation method at ambient pressure, and their refined structure is quite different from other reported ternary M-Te-I phases, which are generally coordination polymers or molecular clusters[33,34]. The powder diffraction pattern of $IrTe_2I$ is shown in **Figure 2A** and its crystallographic information is listed in **Table**

**1**. The crystal structure of $RhTe_2I$ was refined by SXRD (**Tables 2-4**), and Le Bail fitting performed on the PXRD data from the full as-synthesized sample confirms the bulk uniformity (**Figure 2B**).

The materials have a layered structure, made from $MTe_5I$ (M = Ir or Rh) octahedra connected by sharing corners. Revealed by the view along the *c*-axis, it is observed that these layers are double-tiered, through sharing vertices of the octahedra (**Figure 1B**), with iodine mediated Van der Waals interactions between the layers. The layers stack along the *b*-axis of the orthorhombic unit cell, leading to a strong (010) peak at low angle in their PXRD patterns (which can be observed in **Figure 2**). The view along the *b* axis in **Figure 1C** shows that this structure can be considered as resembling a deformed section of the pyrite structural type, as the $MTe_5I$ octahedra form a distorted triangular arrangement of metal cations that is close to being a square net (**Figure 1C** inset). This layered structure in the non-centrosymmetric, non-symmorphic $Pca2_1$ space group thus may attract potential interest, as it can serve as a breeding ground for several potentially interesting properties such as ferroelectricity. The $MTe_5I$ coordination octahedra are slightly distorted for both compounds (especially when compared to the symmetric octahedral coordination environment of $CdI_2$-type $IrTe_2$ with $d_{Ir\text{-}Te}$ = 2.65 Å[35], and pyrite type $RhTe_2$ with $d_{Rh\text{-}Te}$ = 2.65 Å[36]), and the bond lengths between central cations and the anions are listed in **Table 5**. The values of these distances are fairly close when comparing Ir and Rh, suggesting comparable M-X (X = Te or I) bond strengths in the two systems. All of the tellurium atoms are found to be covalently bonded so as to form Te-Te dumbbells in both compounds, with a relatively short Te-Te distance at 2.76 Å in $IrTe_2I$ and 2.82 Å in $RhTe_2I$ (as a comparison, the shortest Te-Te distance is around 2.83 Å in $Ir_3Te_8$, 3.08 Å in pyrite $RhTe_2$, and 2.77 Å in $BaTe_2$[36–38]). This chalcogen dimerization phenomenon is also observed in some other chalcogenide compounds[38–40] resulting in an average chemical valence of -1 for Te in the $MTe_2I$ formula, and thus a +3 valence with $d^6$ electronic configuration for both Ir and Rh. The shortest M-M in-plane distance is 4.39 Å for Ir, and 4.40 Å for Rh (**Figure 1C** inset), and the distance between the two layers is 7.57 Å for Ir and 7.50 Å for Rh, thus it can be seen that $IrTe_2I$ and $RhTe_2I$ have very similar lattice dimensions and interatomic separations. The minor differences may be due to the slight difference between the Ir and Rh atomic radii and electronegativities, which may in turn be attributed to lanthanoid contraction in the sixth row of the periodic table. There is a shorter Te-Te distance and larger interplane spacing in $IrTe_2I$, which suggests stronger bonding of the ditelluride dimer in the system, and weaker interaction between the layers when compared to the Rh variant.

Temperature- and field-dependent magnetization measurements were carried out on the polycrystalline powders of $IrTe_2I$ and $RhTe_2I$. Both compounds show diamagnetic behavior, as shown in **Figure 3A**, as their magnetic susceptibilities are negative under an applied filed of 0.1 T from 1.8 to 300 K. Both materials display a small upturn in susceptibility below 10 K, which we attribute to the presence of very small amounts of paramagnetic impurities. The observed susceptibility is consistent with a low-spin $d^6$ electron configuration of the M(III) ions and supports the existence of the observed Te-Te bonding in the $MTe_2I$ system. The magnetization decreases with increasing magnetic field at both 2 K and 250 K for $IrTe_2I$ and $RhTe_2I$ (**Figure 3A** inset), which is an indication of the diamagnetic nature of the materials.

Temperature dependent resistance measurements were also conducted on as-made dense pieces of the polycrystalline samples (**Figure 3B**). Both compounds show semiconducting behavior, demonstrated by the fact that their resistivities increase with decreasing temperature until the measured values exceed the instrumental limits. Log($\rho$) for both samples is plotted versus $T^{-1}$ in the inset of **Figure 3B**. The transport activation energies ($E_a$) for each compound near ambient temperature can be obtained by fitting the linearly varying parts of the curves to:

$$\rho = \rho_0 e^{-\frac{E_a}{k_B T}} \quad (1)$$

where $\rho_0$ is the pre-exponential term and $k_B$ is Boltzmann's constant. The transport $E_a$s obtained are 0.37 eV for $IrTe_2I$ and 0.25 eV for $RhTe_2I$. The semiconducting nature of the resistivity is consistent with the diffuse reflectance measurements shown in **Figure 3C**.

The wavelength-dependent pseudo absorbance ($A$) data of $IrTe_2I$ and $RhTe_2I$ are presented, as are the Tauc plots for indirect transitions, shown in the inset. Using the equation:

$$Ah\nu = K\,(h\nu - E_g)^n \quad (2)$$

for which $n$ = 0.5 for direct transitions and 2 for indirect transitions, and $K$ is a constant, the indirect band gap value is calculated to be 0.92 eV for $IrTe_2I$ and 0.79 eV for $RhTe_2I$. If instead the transitions are direct, the band gaps are 0.98 eV and 0.74 eV for M = Ir and Rh respectively, which, for present purposes, are not significantly different from the indirect case.

The magnetoresistance (MR) measurements were conducted on a polycrystalline dense sample of $IrTe_2I$ at different temperatures, and the $R$ / $R_0$ values at 300 K and 280 K are plotted versus field in **Figure 4**. (The slight asymmetry of the curves may be due to contributions from the Hall component.) A small negative MR effect of around 1% at 9 T is observed at room temperature. As negative MR effects generally originate from ferromagnetism or in metallic materials, it is surprising that this negative MR behavior is observed in diamagnetic semiconducting $IrTe_2I$ compound. One of the possible explanations is that the weak MR effect is induced by the strong spin orbit coupling (SOC) and non-centrosymmetric nature of the compound. This potential SOC induced MR will be further discussed during the description of the results of the theoretical calculations.

The electronic band structures and corresponding density of states for $IrTe_2I$ and $RhTe_2I$, calculated without and with SOC included, are presented in **Figures 5 and S1.** The crystal structures were optimized prior to band structure calculations in order to find the lowest calculated energies. This optimization results in an increased unit cell size, an extended interlayer distance, and slightly lengthened bonds (especially the Te-Te bond) compared to the experimental structures, with the difference between the experimental and the optimized structures shown in **Figure S2**. The hybridization of the *d*-orbitals of the metals with the *s* and *p* orbitals from I and Te dominates the electronic states near $E_F$ in both cases. $IrTe_2I$ and $RhTe_2I$ are both calculated to be indirect gap semiconductors with band gaps of 0.66 eV and 0.53 eV, respectively. Consistent with the experimentally measured results, the Ir variant has a larger band gap value. The band gap in the Γ-X-S-Y-Γ region of the Brillouin Zone is significantly smaller than the band gap in the Z-U-R-T-Z region, an indication of the stronger intralayer interactions (Γ-X-S-Y-Γ) in the structure. After including SOC in the calculation, the bands split significantly, reducing the calculated band gaps by about ~0.2 eV. The notable change when adding SOC in the calculation also suggests that the strong effect of SOC may be able to induce some unconventional properties, such as the weak negative MR behavior mentioned previously.

## 4. Summary and Conclusion

The previously unreported compounds $IrTe_2I$ and $RhTe_2I$ were synthesized using a solid-state high-pressure method. Their structures were refined by SXRD and laboratory PXRD data, and found to

be layered, with an orthorhombic unit cell in the non-centrosymmetric, non-symmorphic space group $Pca2_1$. Te-Te bonded dimers are seen, leading to a +3 chemical valence with $d^6$ electronic configuration of the metal cations, consistent with the diamagnetic, highly resistive behavior of the two compounds. The semiconducting nature of both compounds is revealed by experimental resistance, diffuse reflectance measurements and theoretical calculations. A weak negative MR effect is observed for $IrTe_2I$, which may be induced by its strong SOC. This MR effect may be of future research interest, and this newly discovered non-centrosymmetric, non-symmorphic layered structure type may inspire future experimental and theoretical exploration and developments in material fabrication and applications of heavy transition metal compounds.

[Deposition number 2167482 for $RhTe_2I$ contains the supplementary crystallographic data from single crystal XRD refinement for this paper, which can be obtained free of charge from The Cambridge Crystallographic Data Centre.]

**Conflict of Interest**

The authors declare no conflict of interest.

**Acknowledgements**

This research was funded by the Gordon and Betty Moore foundation, EPiQS initiative, grant GBMF-9066, by the MRSEC award from NSF Grant DMR 2011750, and by the Arnold and Mabel Beckman Foundation through a Beckman Young Investigator Award to W.X. The single crystal diffraction work at Rutgers University was supported by the U.S. DOE-BES under Contract DE-SC0022156.

**References**

1 M. S. Dresselhaus, G. Chen, M. Y. Tang, R. G. Yang, H. Lee, D. Z. Wang, Z. F. Ren, J.-P. Fleurial and P. Gogna, New Directions for Low-Dimensional Thermoelectric Materials, *Adv. Mater.*, 2007, **19**, 1043–1053.

2 M. Guch, C. Raj Sankar, J. R. Salvador, G. P. Meisner and H. Kleinke, Improvements of the thermoelectric properties of PbTe via simultaneous doping with indium and iodine, *J. Appl. Phys.*, 2012, **111**, 063706.

3 A. Yamashita, Y. Goto, A. Miura, C. Moriyoshi, Y. Kuroiwa and Y. Mizuguchi, n-Type thermoelectric metal chalcogenide (Ag,Pb,Bi)(S,Se,Te) designed by multi-site-type high-entropy alloying, *Mater. Res. Lett.*, 2021, **9**, 366–372.

4 B. M. Başol and B. McCandless, Brief review of cadmium telluride-based photovoltaic technologies, *J. Photonics Energy*, 2014, **4**, 040996.

5 A. Singh, K. M. Boopathi, A. Mohapatra, Y. F. Chen, G. Li and C. W. Chu, Photovoltaic Performance of Vapor-Assisted Solution-Processed Layer Polymorph of $Cs_3Sb_2I_9$, *ACS Appl. Mater. Interfaces*, 2018, **10**, 2566–2573.

6 G. Chen, Y. Yu, K. Zheng, T. Ding, W. Wang, Y. Jiang and Q. Yang, Fabrication of Ultrathin $Bi_2S_3$ Nanosheets for High-Performance, Flexible, Visible–NIR Photodetectors, *Small*, 2015, **11**, 2848–2855.

7 H. Wang, G. Chen, J. Xu, Y. Xu and Q. Yang, Effective Synthesis of $Pb_5S_2I_6$ Crystals at Low Temperature for Fabrication of a High Performance Photodetector, *Cryst. Growth Des.*, 2018, **18**, 1987–1994.

8 H. L. Zhuang, V. R. Cooper, H. Xu, P. Ganesh, R. G. Hennig and P. R. C. Kent, Rashba effect in single-layer antimony telluroiodide SbTeI, *Phys. Rev. B*, 2015, **92**, 115302.

9 R. Yadav, N. A. Bogdanov, V. M. Katukuri, S. Nishimoto, J. van den Brink and L. Hozoi, Kitaev exchange and field-induced quantum spin-liquid states in honeycomb α-$RuCl_3$, *Sci. Rep.*, 2016, **6**, 37925.

10 X. Y. Pu, K. Zhao, Y. Liu, Z. T. Wei, R. Jin, X. S. Yang and Y. Zhao, Structural and transport properties of iridium-doped $Bi_2Se_3$ topological insulator crystals, *J. Alloys Compd.*, 2017, **694**, 272–275.

11 H. Okazaki, K. Terashima, D. Billington, K. Iwata, T. Wakita, M. Tanaka, Y. Takano, Y. Muraoka and T. Yokoya, Change in the electronic structure of the bismuth chalcogenide superconductor $CsBi_{4-x}Pb_xTe_6$ by dissociation of the bismuth dimers, *J. Phys. Condens. Matter*, 2020, **32**, 145501.

12 K. F. Mak, K. He, C. Lee, G. H. Lee, J. Hone, T. F. Heinz and J. Shan, Tightly bound trions in monolayer $MoS_2$, *Nat. Mater.*, 2013, **12**, 207–211.

13 M. A. McGuire, Crystal and Magnetic Structures in Layered, Transition Metal Dihalides and Trihalides, *Crystals*, 2017, **7**, 121.

14 T. Kong, K. Stolze, E. I. Timmons, J. Tao, D. Ni, S. Guo, Z. Yang, R. Prozorov and R. J. Cava, $VI_3$—a New Layered Ferromagnetic Semiconductor, *Adv. Mater.*, 2019, **31**, 1808074.

15 D. Ni, X. Gui, K. M. Powderly and R. J. Cava, Honeycomb-Structure $RuI_3$, A New Quantum Material Related to α-$RuCl_3$, *Adv. Mater.*, 2022, **34**, 2106831.

16 Y. Qi, S. Matsuishi, J. Guo, H. Mizoguchi and H. Hosono, Superconductivity in Defective Pyrite-Type Iridium Chalcogenides $Ir_xCh_2$ (Ch = Se and Te), *Phys. Rev. Lett.*, 2012, **109**, 217002.

17 B. Rasche, A. Isaeva, A. Gerisch, M. Kaiser, W. Van den Broek, C. T. Koch, U. Kaiser and M. Ruck, Crystal Growth and Real Structure Effects of the First Weak 3D Stacked Topological Insulator $Bi_{14}Rh_3I_9$, *Chem. Mater.*, 2013, **25**, 2359–2364.

18 S.-H. Baek, S.-H. Do, K.-Y. Choi, Y. S. Kwon, A. U. B. Wolter, S. Nishimoto, J. van den Brink and B. Büchner, Evidence for a Field-Induced Quantum Spin Liquid in α-$RuCl_3$, *Phys. Rev. Lett.*, 2017, **119**, 037201.

19 Y. Imai, K. Nawa, Y. Shimizu, W. Yamada, H. Fujihara, T. Aoyama, R. Takahashi, D. Okuyama, T. Ohashi, M. Hagihala, S. Torii, D. Morikawa, M. Terauchi, T. Kawamata, M. Kato, H. Gotou, M. Itoh, T. J. Sato and K. Ohgushi, Zigzag magnetic order in the Kitaev spin-liquid candidate material $RuBr_3$ with a honeycomb lattice, *Phys. Rev. B*, 2022, **105**, L041112.

20 J. V. Badding, High-pressure synthesis, characterization, and tuning of solid state materials, *Annu. Rev. Mater. Sci.*, 1998, **28**, 631–658.

21 H. Hegger, C. Petrovic, E. G. Moshopoulou, M. F. Hundley, J. L. Sarrao, Z. Fisk and J. D. Thompson, Pressure-Induced Superconductivity in Quasi-2D $CeRhIn_5$, *Phys. Rev. Lett.*, 2000, **84**, 4986–4989.

22 L. Yang, Y. Zhang, J. Wang, Y. Wang and W. W. Yu, Pressure-induced phase transitions of lead iodide, *RSC Adv.*, 2016, **6**, 84604–84609.

23 D. Ni, S. Guo, K. M. Powderly, R. Zhong and R. J. Cava, A high-pressure phase with a non-centrosymmetric crystal structure in the PbSe–$PbBr_2$ system, *J. Solid State Chem.*, 2019, **280**, 120982.

24 G. M. Sheldrick, Crystal structure refinement with *SHELXL*, *Acta Crystallogr. Sect. C Struct. Chem.*, 2015, **71**, 3–8.

25 N. Walker and D. Stuart, An empirical method for correcting diffractometer data for absorption effects, *Acta Crystallogr. A*, 1983, **39**, 158–166.

26 J. Tauc, R. Grigorovici and A. Vancu, Optical Properties and Electronic Structure of Amorphous Germanium, *Phys. Status Solidi B*, 1966, **15**, 627–637.

27 P. E. Blöchl, Projector augmented-wave method, *Phys. Rev. B*, 1994, **50**, 17953–17979.

28 G. Kresse and J. Furthmüller, Efficiency of ab-initio total energy calculations for metals and semiconductors using a plane-wave basis set, *Comput. Mater. Sci.*, 1996, **6**, 15–50.

29 J. P. Perdew, K. Burke and M. Ernzerhof, Generalized Gradient Approximation Made Simple, *Phys. Rev. Lett.*, 1996, **77**, 3865–3868.

30 H. J. Monkhorst and J. D. Pack, Special points for Brillouin-zone integrations, *Phys. Rev. B*, 1976, **13**, 5188–5192.

31 J. Liu and D. Vanderbilt, Weyl semimetals from noncentrosymmetric topological insulators, *Phys. Rev. B*, 2014, **90**, 155316.

32 J. Cano, B. Bradlyn, Z. Wang, L. Elcoro, M. G. Vergniory, C. Felser, M. I. Aroyo and B. A. Bernevig, Topology of Disconnected Elementary Band Representations, *Phys. Rev. Lett.*, 2018, **120**, 266401.

33 A. Günther and M. Ruck, Hexatellurium Rings in Coordination Polymers and Molecular Clusters: Synthesis and Crystal Structures of $[M(Te_6)]X_3$ (M = Rh, Ir; X = Cl, Br, I) and $[Ru_2(Te_6)](TeBr_3)_4(TeBr_2)_2$, *Z. Für Anorg. Allg. Chem.*, 2012, **638**, 317–323.

34 A. Günther, A. Isaeva and M. Ruck, Stabilization of Decatellurium Molecules in Isolated and Concatenated Clusters, *Z. Für Anorg. Allg. Chem.*, 2013, **639**, 254–260.

35 S. Jobic, P. Deniard, R. Brec, J. Rouxel, A. Jouanneaux and A. N. Fitch, Crystal and electronic band structure of $IrTe_2$: Evidence of anionic bonds in a CdI2-like arrangement, *Z. Für Anorg. Allg. Chem.*, 1991, **598**, 199–215.

36 S. Geller, The Crystal Structures of RhTe and $RhTe_2$, *J. Am. Chem. Soc.*, 1955, **77**, 2641–2644.

37 S. Jobic, M. Evain, R. Brec, P. Deniard, A. Jouanneaux and J. Rouxel, Crystal structure of polymeric pyrite type $Ir_3Te_8$, *J. Solid State Chem.*, 1991, **95**, 319–326.

38 J. Li, H.-Y. Guo, J. R. Carey, S. Mulley, D. M. Proserpio and A. Sironi, Synthesis and crystal structure of a new alkaline-earth metal chalcogenide: Barium ditelluride, *Mater. Res. Bull.*, 1994, **29**, 1041–1048.

39 M. Bremholm, Y. S. Hor and R. J. Cava, Pressure stabilized Se–Se dimer formation in $PbSe_2$, *Solid State Sci.*, 2011, **13**, 38–41.

40 D. Ni, S. Guo, K. M. Powderly, R. Zhong, J. Lin, T. Kong, F. Alex Cevallos and R. J. Cava, Crystal structure and elementary properties of $PbS_2$ with a pressure–stabilized S-S dimer, *J. Solid State Chem.*, 2019, **269**, 442–446.
41 A. Authier, Ed., *International Tables for Crystallography, Physical Properties of Crystals: Physical Properties of Crystals*, John Wiley and Sons, 2nd edition., 2014, vol. D.

**Table 1.** Structural parameters and standardized crystallographic positions of $IrTe_2I$, from the Rietveld refinement of laboratory powder X-ray diffraction data collected at 300 K. Standard deviations are presented in the brackets.

| **Refined Formula** | **$IrTe_2I$** |
|---|---|
| F.W. (g/mol) | 574.32 |
| Space group; Z | $P\,ca2_1$; 4 |
| *a*(Å) | 6.36195(15) |
| *b*(Å) | 10.57425(24) |
| *c*(Å) | 6.40453(15) |
| V (Å$^3$) | 430.851(27) |

| **Atom** | **Wyck.** | **Occ.** | ***x*** | ***y*** | ***z*** | ***$U_{iso}$* equiv.** [Å$^2$] |
|---|---|---|---|---|---|---|
| Ir | 4*a* | 1 | 0. 0141 (4) | 0. 1418 (2) | 0.0000 | 0.0050 (8) |
| Te1 | 4*a* | 1 | 0. 6238 (6) | 0.0829 (3) | 0.1170 (4) | 0.0041 (14) |
| Te2 | 4*a* | 1 | 0.1221 (6) | 0.2341 (3) | 0.3646 (5) | 0.0060 (13) |
| I | 4*a* | 1 | 0.0885 (5) | 0.6185 (3) | 0.3833 (4) | 0.0233 (15) |

**Table 2.** Single crystal structure refinement for $RhTe_2I$ at 293 (2) K. Standard deviations are presented in the brackets.

| **Refined Formula** | **$RhTe_2I$** |
|---|---|
| Temperature (K) | 293 (2) |
| F.W. (g/mol) | 485.01 |
| Space group; Z | $Pca2_1$; 4 |
| *a*(Å) | 6.368 (1) |
| *b*(Å) | 10.562 (2) |
| *c*(Å) | 6.416 (1) |
| V (Å$^3$) | 431.5 (2) |
| θ range (º) | 3.736-31.476 |
| No. reflections; $R_{int}$ | 6055; 0.0322 |
| No. independent reflections | 1425 |
| No. parameters | 15 |
| $R_1$: $\omega R_2$ ($I$>2d($I$)) | 0.0341; 0.0687 |
| Goodness of fit | 1.354 |
| Diffraction peak and hole ($e^-$/ Å$^3$) | 2.038; -1.986 |
| Flack parameter | 0.40 (11) |

**Table 3.** Standardized atomic coordinates and equivalent isotropic displacement parameters for $RhTe_2I$ at 293 (2) K. ($U_{eq}$ is defined as one-third of the trace of the orthogonalized $U_{ij}$ tensor (Å$^2$)) Standard deviations are presented in the brackets.

| **Atom** | **Wyck.** | **Occ.** | ***x*** | ***y*** | ***z*** | $U_{eq}$ |
|---|---|---|---|---|---|---|
| Rh | 4*a* | 1 | 0.0135 (2) | 0.1449 (1) | 0.0000 | 0.0079 (2) |
| Te1 | 4*a* | 1 | 0.6265 (1) | 0.0804 (1) | 0.1193 (1) | 0.0088 (2) |
| Te2 | 4*a* | 1 | 0.1232 (1) | 0.2366 (1) | 0.3634 (1) | 0.0099 (2) |
| Ir | 4*a* | 1 | 0.0834 (2) | 0.6162 (1) | 0.3812 (2) | 0.0164 (2) |

**Table 4.** Anisotropic thermal displacement parameters for $RhTe_2I$ at 293 (2) K. Standard deviations are presented in the brackets.

| **Atom** | **U11** | **U22** | **U33** | **U12** | **U13** | **U23** |
|---|---|---|---|---|---|---|
| Rh | 0.0064 (4) | 0.0108 (4) | 0.0063 (3) | -0.0005 (4) | 0.0003 (4) | 0.0002 (3) |
| Te1 | 0.0063 (3) | 0.0126 (4) | 0.0075 (3) | 0.0010 (3) | 0.0010 (3) | 0.0008 (3) |
| Te2 | 0.0084 (3) | 0.0136 (4) | 0.0077 (3) | 0.0002 (3) | 0.0004 (4) | 0.0002 (3) |
| I | 0.0176 (4) | 0.0145 (4) | 0.0172 (4) | -0.0024 (4) | 0.0015 (4) | 0.0030 (3) |

*For an explanation of the anisotropic thermal displacement parameters, see *The International Tables for Crystallography*, A. Authier editor, second edition, volume D, pages 231 to 245, John Wiley and Sons, 2014.[41]

**Table 5.** Selected bond lengths (Å) for **M**$Te_2I$ with **M** = Ir or Rh. Standard deviations are presented in the brackets.

| **Bonds** | **$IrTe_2I$** | **$RhTe_2I$** |
|---|---|---|
| **M**-Te | 2.587(4) | 2.6012(15) |
| | 2.622(5) | 2.6198(16) |
| | 2.657(5) | 2.6570(15) |
| | 2.668(5) | 2.6685(15) |
| | 2.679(4) | 2.6877(16) |
| **M**-I | 2.721(4) | 2.7073(16) |
| Te-Te | 2.760(5) | 2.8187(13) |

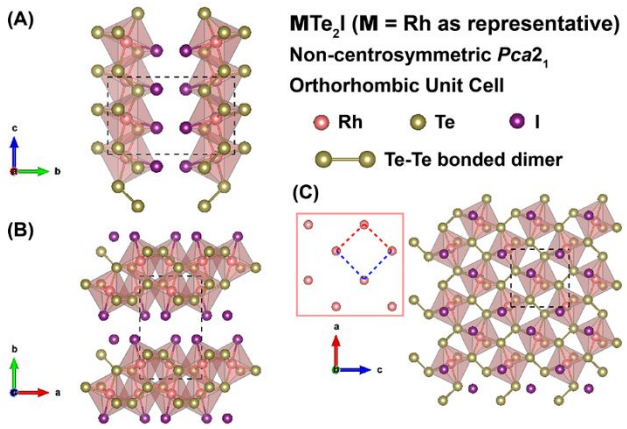


**Figure 1. The non-centrosymmetric crystal structures of high-pressure-synthesized $IrTe_2I$ and $RhTe_2I$** with the structure of $RhTe_2I$ presented in this figure as the representative of the two isostructural compounds. Views along the (A) *a*-axis, (B) *c*-axis, and (C) the layer stacking direction *b*-axis are exhibited respectively. Te-Te bonded dimers can be clearly observed through the different views of the structure. The inset in (C) reveals the in-plane arrangement of metal cation lattice, with M-M distance at 4.40 Å (red dashed line, shorter) and 4.64 Å (blue dashed line, longer) in $RhTe_2I$. These distances are 4.39 Å and 4.64 Å respectively when M = Ir.

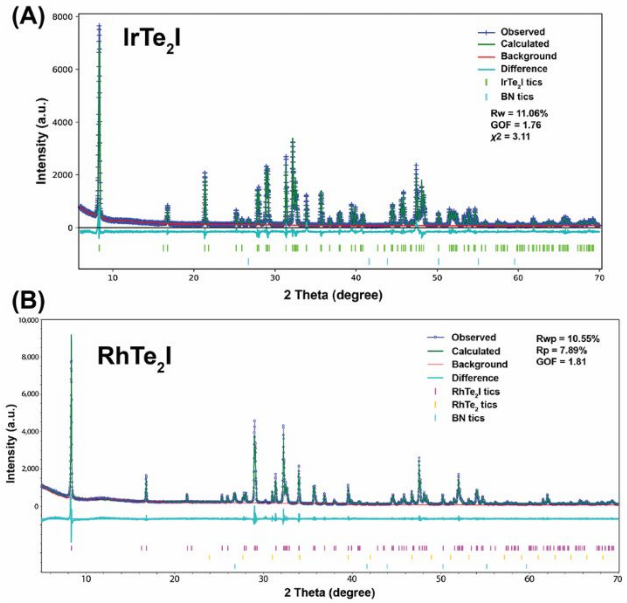


**Figure 2. Ambient Temperature Powder X-ray Diffraction Data for the two materials.** (A) Rietveld refinement of the laboratory PXRD pattern of $IrTe_2I$; (B) Le Bail fit of the laboratory PXRD pattern of $RhTe_2I$. A small amount of $RhTe_2$ is found as an impurity in the $RhTe_2I$ product.

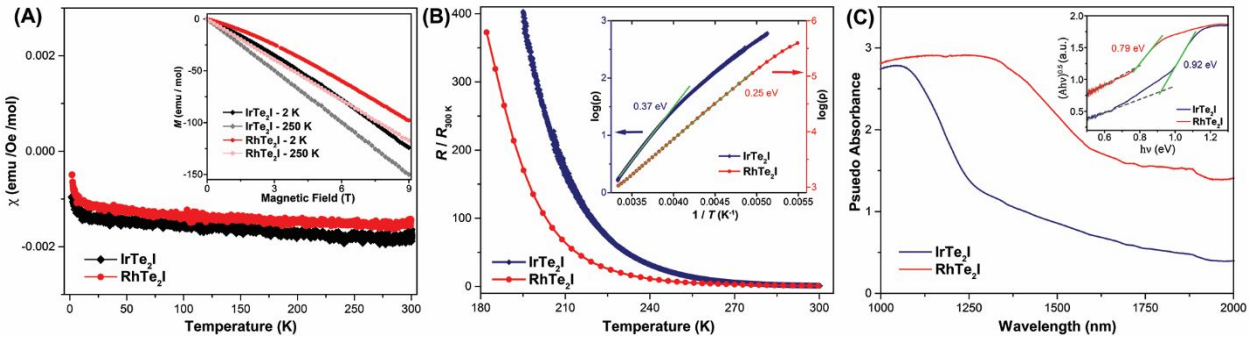


**Figure 3. Basic magnetic, electrical and optical absorption characterization of $IrTe_2I$ and $RhTe_2I$.** (A) Temperature-dependent magnetic susceptibilities measured on polycrystalline powder samples from 1.8 to 300 K, with the inset presenting field-dependent magnetization measurements from 0 to 9 T at two different temperatures for each sample; (B) Resistance measured from 180 to 300 K on as-made dense samples, where $R_{300\ K}$ represents the resistance at 300 K. The inset shows the log($\rho$) of both samples ($IrTe_2I$ on left *y*-axis and $RhTe_2I$ on right *y*-axis), plotted versus $T^{-1}$, with the linear fitting (green lines) on the higher temperature range of each curve employed to calculate the charge transport activation energy; (C) Pseudo Kubelka-Munk absorbance spectra (main panel) and the Tauc plot for the indirect optical transitions (inset) for polycrystalline samples**.** The optical band gap values are estimated by extrapolating the intersection of the green lines (the linear absorption region) and the gray dashed lines (absorption baseline).

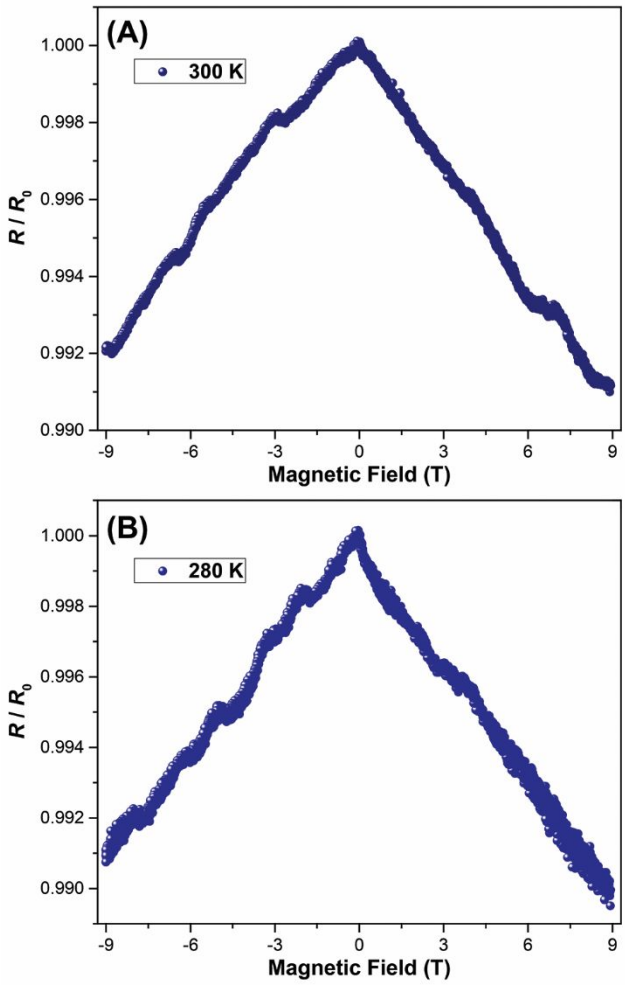


**Figure 4. Magnetoresistance measurements on a polycrystalline dense piece of $IrTe_2I$** at (A) 300 K and (B) 280 K, under an applied magnetic field swept from 9 T to -9 T. $R_0$ is the resistance under zero applied field. The excitation voltage is 5 V.

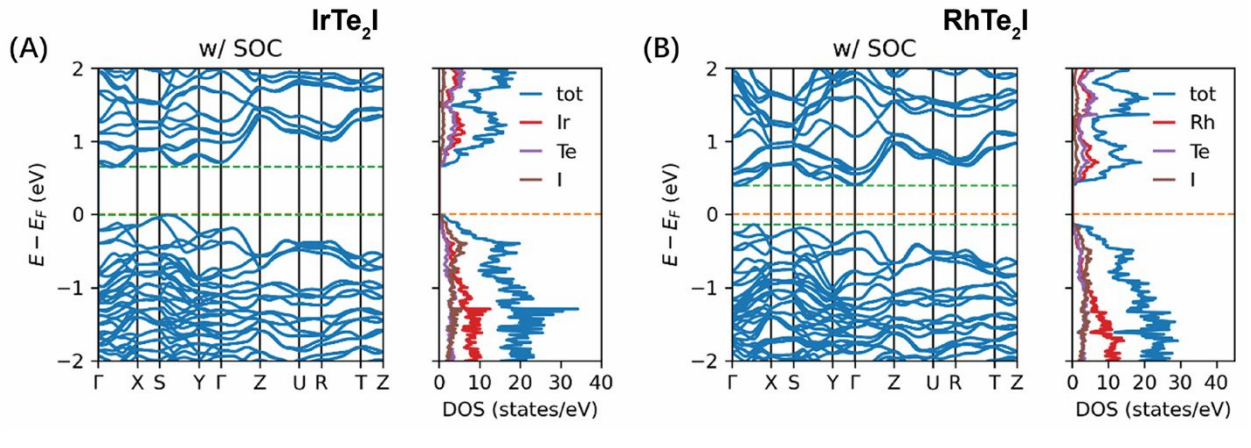


**Figure 5. The Calculated electronic band structures and DOS** for (A) $IrTe_2I$ and (B) $RhTe_2I$ with SOC included. Fermi level ($E_F$), conduction band minimum (CBM), and valence band maximum (VBM) are highlighted by orange dash lines and green dash lines.